

OCEANOGRAPHY

Glacial cycles drive variations in the production of oceanic crust

John W. Crowley,^{1,2*} Richard F. Katz,^{1†} Peter Huybers,²
Charles H. Langmuir,² Sung-Hyun Park^{3†}

Glacial cycles redistribute water between oceans and continents, causing pressure changes in the upper mantle, with consequences for the melting of Earth's interior. Using Plio-Pleistocene sea-level variations as a forcing function, theoretical models of mid-ocean ridge dynamics that include melt transport predict temporal variations in crustal thickness of hundreds of meters. New bathymetry from the Australian-Antarctic ridge shows statistically significant spectral energy near the Milankovitch periods of 23, 41, and 100 thousand years, which is consistent with model predictions. These results suggest that abyssal hills, one of the most common bathymetric features on Earth, record the magmatic response to changes in sea level. The models and data support a link between glacial cycles at the surface and mantle melting at depth, recorded in the bathymetric fabric of the sea floor.

The bathymetry of the sea floor has strikingly regular variations around intermediate and fast-spreading ocean ridges. Parallel to the ridge are long, linear features with quasi-regular spacing called abyssal hills (1). High-resolution mapping of the sea floor over the past few decades (2–4) has shown that these hills are among the most common topographic features of the planet, populating the sea floor over ~50,000 km of ridge length. Hypothesized models for these features include extensional faulting parallel to the ridge (3), variations in the magmatic budget of ridge volcanoes (5), and variation in mantle melting under ridges owing to sea-level change associated with glacial cycles (6). This latter model stems from the fact that glacial-interglacial variations transfer $\sim 5 \times 10^{19}$ kg of water between the oceans and the continents. This mass redistribution translates to sea-level variations of ~100 m and modifies the lithostatic pressure beneath the entire ocean. Because mantle melting beneath ridges is driven by depressurization, ocean ridge volcanism should respond to sea-level changes, potentially leading to changes in the thickness and elevation of ocean crust.

Plate spreading at mid-ocean ridges draws mantle flow upward beneath the ridge; rising parcels of mantle experience decreasing pressure and hence decreasing melting point, causing partial melting. Mantle upwelling rates are ~3 cm/year on average, whereas sea-level change during the last deglaciation was at a mean rate of 1 cm/year over 10 thousand years (ky). Because water has one third the density of rock, sea-level changes would modify the depressurization rate associated with upwelling by $\pm 10\%$, with corresponding effects on the rate of melt production. Mantle

upwelling rate scales with the mid-ocean ridge spreading rate, but the rate of sea-level change over the global mid-ocean ridge system is roughly uniform. On this basis, previous workers inferred that the relative effect of sea-level change should scale inversely with spreading rate, reaching a maximum at the slowest rates (6). An elaboration of this model with parameterized melt transport gave a similar scaling (7).

To test these qualitative inferences, we investigated the crustal response to sea-level change

using a model that computes mantle flow, thermal structure, melting, and pathways of melt transport. The model is based on canonical statements of conservation of mass, momentum, and energy for partially molten mantle (8, 9) and has previously been used to simulate mid-ocean ridge dynamics with homogeneous (10) and heterogeneous (11) mantle composition. It predicts time scales of melt transport that are consistent with those estimated from ²³⁰Th disequilibrium in young lavas (12). In the present work, the model is used to predict crustal thickness time series arising from changes in sea level (Fig. 1) (13).

A suite of nine model runs for three permeability scales and three spreading rates was driven over a 5-million-year period by using a Plio-Pleistocene sea-level reconstruction (14). Crustal curves from simulations with larger permeability and faster spreading rate contain relatively more high-frequency content than those of lower permeability and slower-spreading-rate runs (Fig. 1). Our model results contradict the previous scaling arguments (6, 7) in not showing a simple decrease in the sea-level effect on ridge magmatism with increasing spreading rate.

To better understand these numerical results, we carried out an analysis of leading-order processes using a reduced complexity model. This model provides a solution for crustal thickness response to changes in sea level, approximating the results of the full numerical model, but with greater transparency. Assuming that all melt produced by sea-level change is focused to the

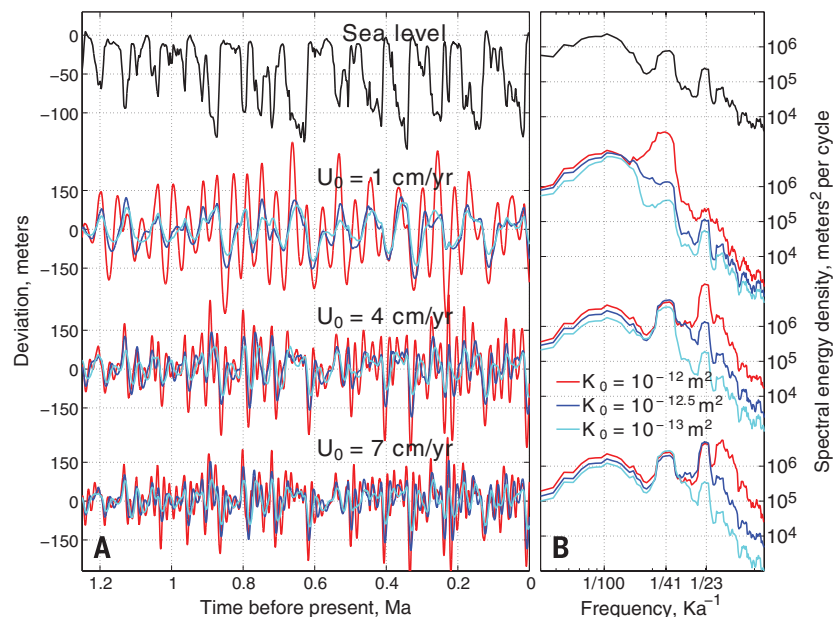


Fig. 1. Simulated bathymetric relief driven by Plio-Pleistocene sea-level variation. (A) Imposed sea-level variation [black, from (14)] and predicted bathymetric relief (color) for the past 1.25 million years from simulations at three half-spreading rates U_0 and three permeability levels K_0 . Isostatic compensation is assumed to scale the amplitude of crustal thickness variation by 6/23 to give bathymetric relief. Permeability in the simulations is computed by applying $K(x,z) = K_0(\phi/\phi_0)^3 m^2$ to the porosity field $\phi(x,z)$, where $\phi_0 = 0.01$ is a reference porosity. Light blue, dark blue, and red lines correspond to $\log_{10} K_0 = (-13, 12.5, 12)$, respectively. (B) Power spectral density estimates for each time series, made by using the multitaper method with seven tapers. Axes are logarithmic.

¹Department of Earth Sciences, University of Oxford, Oxford, UK. ²Department of Earth and Planetary Sciences, Harvard University, Cambridge, USA. ³Division of Polar Earth-System Sciences, Korea Polar Research Institute, Incheon, Korea. *Present address: Engineering Seismology Group Canada, Kingston, Canada. †Corresponding author. E-mail: richard.katz@earth.ox.ac.uk (R.F.K.); shpark314@kopri.re.kr (S.-H. P.)

ridge axis, we obtain a magmatic flux in units of kilograms per year per meter along the ridge of

$$M_{SL}(t) = \int_{z_m}^0 x_l(z) \frac{\rho_w}{\rho_m} \Pi \dot{S}[t - \tau(z)] dz \quad (1)$$

where ρ_w/ρ_m is the density ratio of sea water to mantle rock, Π is the adiabatic productivity of upwelling mantle (in kilograms of melt per cubic meter of mantle per meter of upwelling), $x_l(z)$ is the half-width of the partially molten region beneath the mid-ocean ridge at a depth z , z_m is the maximum depth of silicate melting beneath the ridge, and $\dot{S}[t - \tau(z)]$ is the rate of sea-level change τ years before time t (13).

This formulation reveals why our numerical model results (Fig. 1) contradict earlier work (6, 7). Whereas earlier work noted that variations in crustal thickness are inversely proportional to spreading rate, $C_{SL} = M_{SL}/(U_0\rho_c)$, our model shows that mass flux is proportional to the width of the partially molten region beneath the ridge. This width can be expressed as $x_l(z) = U_0R(z)/(4\kappa)$, where U_0 is the half-spreading rate, κ is the thermal diffusivity, and $R(z)$ accounts for depth-dependent influences on melting that are independent of spreading rate (fig. S1). The competing influences associated with the volume of mantle from which melt is extracted and the rate at which new crust is formed means that sensitivity to sea-level variation does not simply decrease with increasing spreading rate.

Instead, the magnitude of the crustal response depends on the time scale of sea-level forcing relative to the time required to deliver melt from depth to the surface. Melt delivery times τ are computed in the reduced model by using a one-dimensional melt column formulation and decrease with higher permeability and faster spreading rate (13, 15). The same response occurs in the numerical model; in both cases, τ decreases with increasing spreading rate because the background melting rate, dynamic melt fraction, and permeability of the melting region all increase.

To quantify crustal response as a function of time scale, we use the amplitude ratio of crustal to sea-level variation, called admittance, computed at discrete frequencies by applying sinusoidal forcing. Admittance curves for both the numerical (Fig. 2A) and reduced (Fig. 2B) models show a distinct maximum that shifts toward higher frequencies and larger magnitudes with shorter τ . When the period of sea-level forcing is short relative to the characteristic transport time $\tau_m = \tau(z_m)$, additional melt produced at depth (falling sea-level phase) does not have time to reach the surface before a negative perturbation to melt production occurs (rising sea-level phase); positive and negative perturbations cancel, and crustal variation is small. When forcing periods are long relative to τ_m , melt perturbations reach the surface but are again small because melt production scales with the rate-of-change of sea level. Forcing periods near τ_m give maximum admittance because of a combination of large perturbation of melting rates and sufficient time to reach the surface (Fig. 2C). These results suggest that ridges are tuned according to melt-

transport rates to respond most strongly to certain frequencies of sea-level variability.

The correspondence of the results from the numerical and reduced models provides a sound basis for investigating the potential effects of sea-level change on sea-floor bathymetry. Variations in melt production lead to variations in crustal thickness, and through isostatic compensation, such thickness variations should produce changes in bathymetry identifiable in high-resolution surveys. The prominent spectral peaks of late Pleistocene sea-level variation at the approximately $1/100 \text{ ky}^{-1}$ ice age, $1/41 \text{ ky}^{-1}$ obliquity, and $1/23 \text{ ky}^{-1}$ precession frequencies (16) therefore translate into a prediction for a bathymetric response that depends on permeability and spreading rate.

Our model results suggest that the best chance to detect a sea-level response between $1/100 \text{ ky}^{-1}$ to $1/20 \text{ ky}^{-1}$ frequencies is at intermediate spreading ridges. Slow spreading ridges show little precession response, an obliquity response that is sensitive to uncertainties in permeability, and the effects of intense normal faulting. Such faulting causes rift valleys with larger relief than expected from sea level-induced melting variations. The sea-level signal should be less polluted by tectonic effects at fast spreading ridges but may have peak admittances at frequencies higher than

$1/20 \text{ ky}^{-1}$ that would obscure the responses at predicted frequencies. For example, the numerical simulation with the fastest spreading and highest permeability has peak spectral energy at frequencies above precession (Fig. 1B).

At intermediate half-spreading rates of 3 cm/year, 40-ky periods lead to predicted bathymetric variations with a wavelength of 1200 m on each side of the ridge. Such fine-scale variations can be obscured in global topographic databases that grid data from multiple cruises and may have offsets in navigation or depth. To investigate the model predictions, a modern data set with uniform navigation and data reduction from a single survey is preferred. Such data are available for two areas of the Australian-Antarctica ridge that were surveyed by the icebreaker Araon of the Korean Polar Research Institute in 2011 and 2013 (Fig. 3).

Analysis was undertaken by identifying a region whose abyssal hill variability is relatively undisturbed by localized anomalies, averaging off-axis variability into a single bathymetric line and converting off-axis distance into an estimate of elapsed time by using a plate motion solution (17). Spectral analysis of the associated bathymetry time series is performed by using the multitaper procedure (18) and shows spectral peaks that are significant at an ~95% confidence level

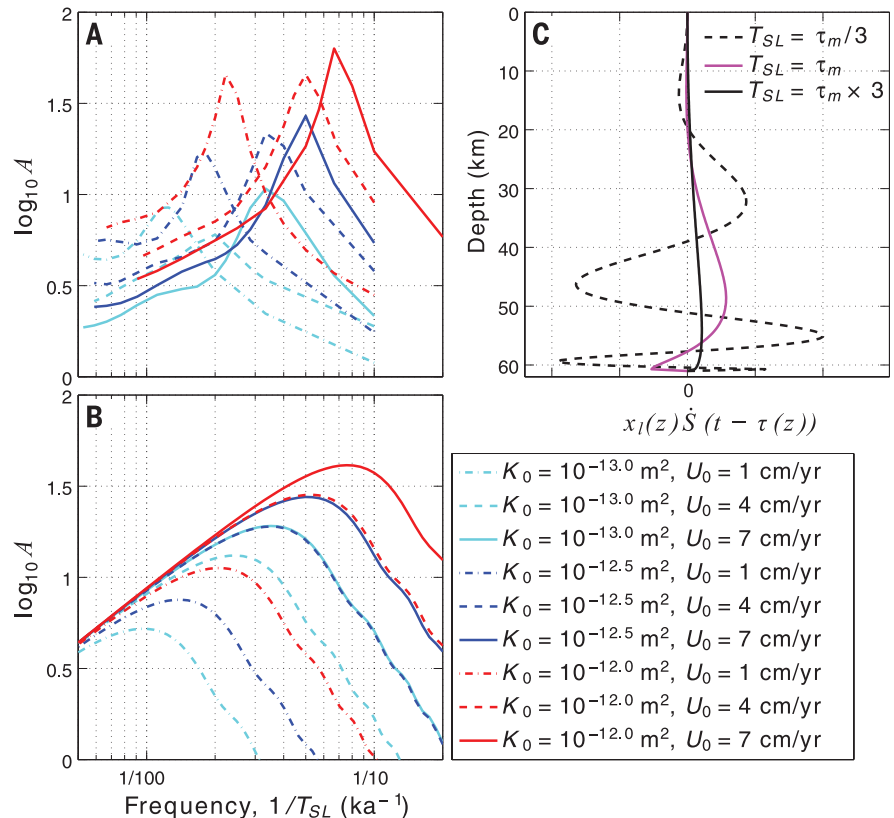


Fig. 2. Crustal thickness admittance, computed for a sinusoidal variation in sea level with period T_{SL} . (A and B) Admittance curves derived from (A) numerical simulations and (B) the reduced model (13). (C) A plot of depth z versus the integrand from the reduced model of magma production owing to sea-level variation, $M_{SL}(t) \propto \int_{z_m}^0 x_l(z) \dot{S}[t - \tau(z)] dz$ (Eq. 1 and text following). The model is evaluated for $U_0 = 4 \text{ cm/year}$, $K_0 = 10^{-13} \text{ m}^2$, and three values of sea-level oscillation period T_{SL} .

near the predicted ice age, obliquity, and precession frequencies (Fig. 3). Although absolute ages are uncertain because we lack sea-floor magnetic reversing data, spectral analysis only requires constraining the relative passage of time. The 2σ uncertainties associated with relative Australian-Antarctic plate motion are $\pm 4\%$ (17), implying, for example, that the $1/41 \text{ ky}^{-1}$ obliquity signal resides in a band from $1/39 \text{ ky}^{-1}$ to $1/43 \text{ ky}^{-1}$, a width that is smaller than our spectral resolution.

Another check on model-data consistency is to compare magnitudes of variability. Surface bathymetry will be roughly $6/23$ ths of the total variation in crustal thickness because of the relative

density differences of crust-water and crust-mantle, assuming conditions of crustal isostasy. The closest match between simulation results and observations, in terms of the distribution of spectral energy, is achieved by specifying a permeability at 1% porosity of $K_0 = 10^{-13} \text{ m}^2$ (Fig. 3). The standard deviation of the simulated bathymetry is 36 m, after multiplying crustal thickness by $6/23$ and filtering (13). To minimize the contribution from non-sea-level-induced variations in the observed bathymetry, it is useful to filter frequencies outside of those between $1/150 \text{ ky}^{-1}$ and $1/10 \text{ ky}^{-1}$. The standard deviation of the filtered observations is 44 m, where the slightly larger

value is consistent with changes in sea level being an important but not exclusive driver of changes in crustal thickness.

Analysis of bathymetry in another area of the Australian-Antarctic ridge 400 km to the southeast (fig. S2) shows a significant spectral peak at the obliquity frequency and indication of a peak near $1/100 \text{ ky}^{-1}$, but no peak near the precession frequencies. Predicted and observed bathymetry is also similar, with standard deviations of 33 and 34 m, respectively, after accounting for fractional surface expression and filtering. Absence of a precession peak may result from spectral estimates being more sensitive to elapsed time errors at higher frequencies (19), where such errors may be introduced through extensional faulting or asymmetric spreading. Detection could also be obscured by the previously noted influence of faulting (3, 20) as well as off-axis volcanism or sediment infilling of abyssal troughs. Detection of significant spectral peaks at predicted frequencies at two locations of the Australian-Antarctic ridge nonetheless constitutes strong evidence for modulation of crustal production by variations in sea level.

Our numerical and analytical results show a complex relationship between spreading rate and amplitudes of crustal thickness variations associated with changes in sea level. Perturbations to the background melt production and delivery depend on the frequency content of the sea-level signal, as a result of the dynamics of magma transport. Reference mantle permeability and ridge-spreading rate are key controls on this frequency dependence. This result could be useful: The spreading rate can be accurately determined for a ridge, but parameters associated with magma dynamics are far less certain, such as the amplitude and scaling of permeability. Uncertainty associated with spectral estimates of bathymetry and sea-level estimates need to be better characterized, but together, these may provide a constraint on the admittance and hence dynamical parameters of a ridge.

Although results from the high-resolution bathymetry are promising, much remains to be done to further test the hypothesis advanced here. Crustal thickness is not an instantaneous response to melt delivery from the mantle but also reflects crustal processes that may introduce temporal and spatial averaging. Where long-lived magma chambers are present, for example, there may also be a crustal time-averaging that depends on spreading rate. In addition, faulting at all spreading rates is an observed and important phenomenon, and sea-floor bathymetry reflects the combined effects of magma output and crustal faulting (3, 20). Deconvolving the relative roles of such processes will be important. High-resolution surveys in targeted regions will provide the opportunity for a more complete and rigorous analysis than is presently possible.

REFERENCES AND NOTES

1. H. Menard, J. Mammerickx, *Earth Planet. Sci. Lett.* **2**, 465–472 (1967).
2. D. Scheirer et al., *Mar. Geophys. Res.* **18**, 1–12 (1996).

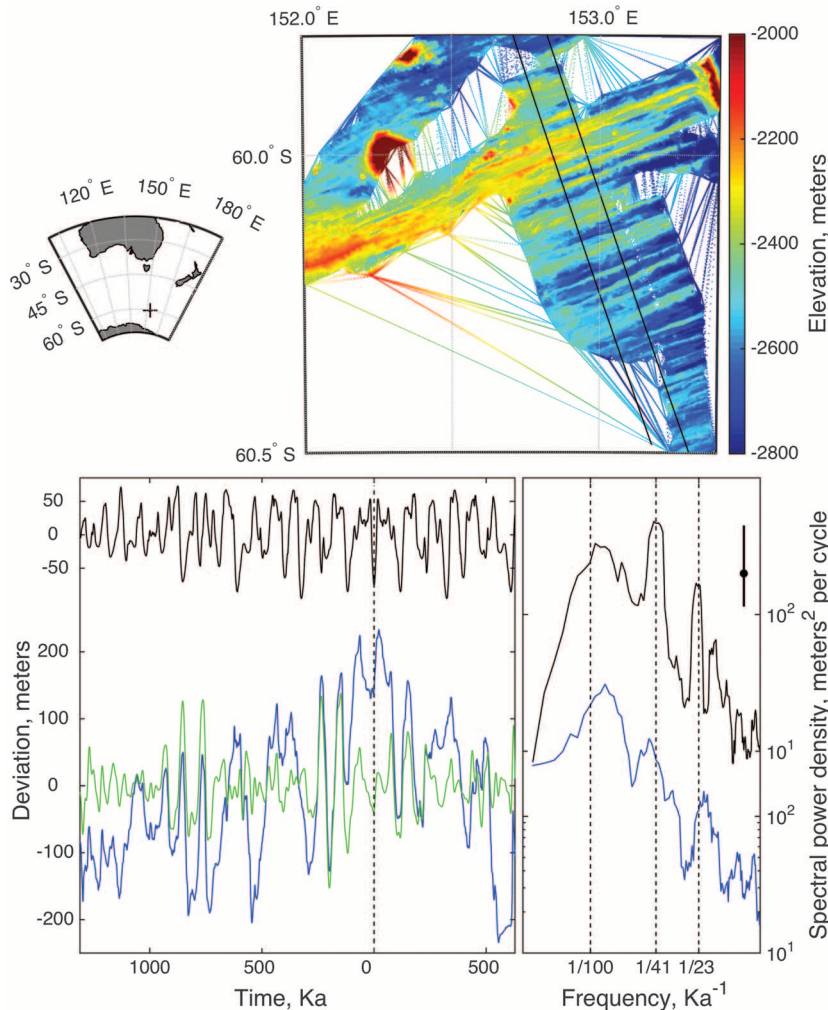


Fig. 3. Bathymetry at a section of the Australian-Antarctic Ridge. A region of consistent bathymetry is indicated between the black lines (top right) and is shown in profile (bottom left, blue) after converting off-axis distance to an estimate of time. Time is zero at the approximate ridge center. Also shown is bathymetry after filtering frequencies outside of $1/150 \text{ ky}$ and $1/10 \text{ ky}$ (green), and simulated bathymetry (black, for $U_0 = 3.3 \text{ cm/year}$ and $K_0 = 10^{-13} \text{ m}^2$). Spectral estimates (bottom right) are shown for the unfiltered bathymetry (blue) and model results (black), where the latter are offset upward by an order of magnitude for visual clarity. Data availability is uneven across the ridge, and spectral estimates are for the longer, southern flank. Unlike in Fig. 1B, spectral estimates are prewhitened in order to improve the detectability of spectral peaks (supplementary materials). Vertical dashed lines indicate frequencies associated with 100-ky late-Pleistocene ice ages, obliquity, and precession. Axes are logarithmic. Statistical significance is indicated by the black bar at the top right; spectral peaks rising further than the distance between the mean background continuum (corresponding to the black dot) and 95th percentile (top of black bar) are significant.

3. K. Macdonald, P. Fox, R. Alexander, R. Pockalny, P. Gente, *Nature* **380**, 125–129 (1996).
4. J. Goff, Y. Ma, A. Shah, J. Cochran, J. Sempere, *J. Geophys. Res.* **102** (B7), 15521 (1997).
5. E. Kappel, W. Ryan, *J. Geophys. Res.* **91** (B14), 13925 (1986).
6. P. Huybers, C. Langmuir, *Earth Planet. Sci. Lett.* **286**, 479–491 (2009).
7. D. C. Lund, P. D. Asimow, *Geochem. Geophys. Geosyst.* **12**, 12009 (2011).
8. D. McKenzie, *J. Petrol.* **25**, 713–765 (1984).
9. R. Katz, *J. Petrol.* **49**, 2099 (2008).
10. R. Katz, *Geochem. Geophys. Geosyst.* **10**, QOAC07 (2010).
11. R. Katz, S. Weatherley, *Earth Planet. Sci. Lett.* **335–336**, 226–237 (2012).
12. A. Stracke, B. Bourdon, D. McKenzie, *Earth Planet. Sci. Lett.* **244**, 97–112 (2006).
13. Materials and methods are available as supplementary materials on Science Online.
14. M. Siddall, B. Hönisch, C. Waelbroeck, P. Huybers, *Quat. Sci. Rev.* **29**, 170–181 (2010).
15. I. Hewitt, *Earth Planet. Sci. Lett.* **300**, 264–274 (2010).
16. J. D. Hays, J. Imbrie, N. J. Shackleton, *Science* **194**, 1121–1132 (1976).
17. C. DeMets, R. G. Gordon, D. F. Argus, *Geophys. J. Int.* **181**, 1–80 (2010).
18. D. Percival, A. Walden, *Spectral Analysis for Physical Applications: Multitaper and Conventional Univariate Techniques* (Cambridge Univ. Press, Cambridge, UK, 1993).
19. P. Huybers, C. Wunsch, *Paleoceanography* **19**, PA1028 (2004).
20. W. R. Buck, L. L. Lavier, A. N. Poliakov, *Nature* **434**, 719–723 (2005).

ACKNOWLEDGMENTS

The research leading to these results has received funding from the European Research Council (ERC) under the European Union's

Seventh Framework Programme (FP7/2007–2013)/ERC grant agreement 279925 and from the U.S. National Science Foundation under grant 1338832. It is a part of project PPI3040 and PEI4050 funded by the Korea Polar Research Institute. J.W.C. thanks J. Mitrovica, and R.F.K. thanks the Leverhulme Trust for additional support. Numerical models were run at Oxford's Advanced Research Computing facility. Bathymetry data are included in the supplementary materials.

SUPPLEMENTARY MATERIALS

www.sciencemag.org/content/347/6227/1237/suppl/DC1

Figs. S1 to S3

Table S1

References (21–29)

Data Files KR1 and KR2

22 September 2014; accepted 28 January 2015

10.1126/science.1261508

EPIDEMIOLOGY

Reduced vaccination and the risk of measles and other childhood infections post-Ebola

Saki Takahashi,¹ C. Jessica E. Metcalf,^{1,2} Matthew J. Ferrari,³ William J. Moss,⁴ Shaun A. Truelove,⁴ Andrew J. Tatem,^{5,6,7} Bryan T. Grenfell,^{1,6} Justin Lessler^{4*}

The Ebola epidemic in West Africa has caused substantial morbidity and mortality. The outbreak has also disrupted health care services, including childhood vaccinations, creating a second public health crisis. We project that after 6 to 18 months of disruptions, a large connected cluster of children unvaccinated for measles will accumulate across Guinea, Liberia, and Sierra Leone. This pool of susceptibility increases the expected size of a regional measles outbreak from 127,000 to 227,000 cases after 18 months, resulting in 2000 to 16,000 additional deaths (comparable to the numbers of Ebola deaths reported thus far). There is a clear path to avoiding outbreaks of childhood vaccine-preventable diseases once the threat of Ebola begins to recede: an aggressive regional vaccination campaign aimed at age groups left unprotected because of health care disruptions.

The current Ebola crisis in West Africa is one of the worst public health disasters in recent memory, having caused more than 21,000 cases and 8400 deaths as of January 2015 and raising the specter of a broader international crisis (1). However, there are signs of hope. Evidence shows that the number of cases is declining in Liberia (2), and sustained transmission has been confined to Guinea, Liberia, and Sierra Leone, despite several transnational introductions including recent transmission in Mali. Stopping Ebola would be a triumph for the global health community and the public health agencies of the affected countries. But even after the last Ebola case recovers, the disruptions of

local health systems caused by the outbreak could lead to a second infectious disease crisis that could kill as many as, if not more than, the original outbreak.

Through the combination of the World Health Organization (WHO) Expanded Programme on Immunization (EPI) and periodic supplemental immunization campaigns, annual childhood deaths from vaccine-preventable diseases have dropped from an estimated 900,000 in 2000 to 400,000 in 2010 (3). Measles is emblematic of this success; globally, estimated annual measles mortality has decreased from 499,000 to 102,000 since 2000 (4, 5). The Ebola-affected countries have been an important part of this achievement: The three countries reported nearly 93,685 cases of measles in the decade between 1994 and 2003 (despite Sierra Leone not reporting in 4 years), and only 6937 between 2004 and 2013 (in both periods it is likely that only a fraction of measles cases were reported to the WHO) (6). Despite this success, measles susceptibility has been growing in all three countries in recent years, and each had planned a measles vaccination campaign prior to the Ebola outbreak.

Measles epidemics often follow humanitarian crises. Measles is one of the most transmissible infections, and immunization rates tend to be lower than for other EPI vaccines, in part because of the older age at which measles vaccine must be administered [9 months, versus 6 weeks or younger for the first dose of other vaccines (7)]. For this reason, explosive measles outbreaks are often an early result of health system failure. Outbreaks have followed disruptions due to war [e.g., the current conflict in Syria (8)], natural disasters [e.g., the eruptions of Mt. Pinatubo in 1991 (9)], and political crises [e.g., Haiti in the early 1990s (10)]. The effects are most acute when measles epidemics are associated with famine or long-term national instability: A survey of 595 households displaced as a result of the Ethiopian famine in 2000 found measles to be a contributing cause in 35 of 159 deaths (11), and after years of instability in the Democratic Republic of Congo, the country experienced a measles outbreak of 294,455 cases and 5045 deaths between 2010 and 2013 (12).

To understand how Ebola-related health care disruptions are increasing the risk from measles, we estimated the spatial distribution of unvaccinated children and the measles susceptibility profile for each country before and after these disruptions. Geolocated cross-sectional data from Demographic and Health Surveys (DHS) in Guinea, Liberia, Sierra Leone, and surrounding countries were used to estimate vaccine coverage in each 5 km × 5 km grid cell by means of a hierarchical Bayesian model and spatial smoothing techniques. These rates were applied to spatially explicit data on population and birth cohort size to map the number of children between 9 months and 5 years of age who were unvaccinated against measles before Ebola-related health care disruptions (Fig. 1A) (13, 14). Forward projections of the number of unvaccinated children after 6, 12, and 18 months were generated by reducing the rate of routine vaccination by 75% for the specified duration (reductions of 25, 50, and 100% were also considered as a sensitivity analysis). Full population susceptibility on a national level at baseline and after 18 months of disruptions were then estimated by combining these estimates with the results of models that estimate the immune profile in each age cohort on the basis of their

¹Department of Ecology and Evolutionary Biology, Princeton University, Princeton, NJ 08544, USA. ²Woodrow Wilson School, Princeton University, Princeton, NJ 08544, USA.

³Centre for Infectious Disease Dynamics, Pennsylvania State University, State College, PA 16801, USA. ⁴Department of Epidemiology, Johns Hopkins Bloomberg School of Public Health, Baltimore, MD 21205, USA. ⁵Department of Geography and Environment, University of Southampton, Southampton SO17 1BJ, UK. ⁶Fogarty International Center, National Institutes of Health, Bethesda, MD 20892, USA.

⁷Flowminder Foundation, 17177 Stockholm, Sweden.

*Corresponding author. E-mail: justin@jhu.edu



www.sciencemag.org/cgi/content/full/science.1261508/DC1

Supplementary Material for

Glacial cycles drive variations in the production of oceanic crust

John W. Crowley, Richard F. Katz, Peter Huybers, Charles H. Langmuir,
Sung-Hyun Park*

*Corresponding author. E-mail: Richard.Katz@earth.ox.ac.uk (R.F.K.); shpark314@kopri.re.kr (S.-H. P.)

Published 5 February 2015 on *Science* Express
DOI: 10.1126/science.1261508

This PDF file includes:

Figs. S1 to S3
Table S1
Full Reference List

Other Supplementary Material for this manuscript includes the following:
(available at www.sciencemag.org/content/science.1261508/DC1)

Data Files KR1 and KR2 as separate gzipped archives

Supplementary text

A The numerical model

A numerical model that self-consistently computes mantle flow, thermal structure, pressure- and temperature-dependent melting, and magmatic segregation/transport provides a context to test the hypotheses considered here. The model is built on a theoretical framework of conservation of mass, momentum, and energy for the magma/mantle system (8, 9, 21); it has been implemented in computational simulations of mid-ocean ridges with homogeneous (10) and heterogeneous (11) mantle. In the present work, the same code is used with minor modifications. The most important change is that the lithostatic pressure at any point in the two-dimensional domain is now augmented with a time-dependent overburden representing sea level. As discussed in detail below, this is a small perturbation to the pressure, and hence the gross behavior of the model is unaffected. Crucially, melt that is generated within the melting regime beneath the ridge rises due to its buoyancy; some of this melt is focused toward the ridge axis. Melt is removed from the domain at the ridge axis through an internal boundary representing a sill, just below the depth where temperatures cross the solidus. Magma percolates upward into the sill, driven by buoyancy, and is instantaneously extracted and added to the crust. Predicted crustal thickness is recorded after each time-step.

The petrological model of magma genesis follows exactly from ref. (10); melting is computed based on a linearized, two-component phase diagram under the assumption of equilibrium thermodynamics. The two components represent fertile and refractory end-member compositions, rather than particular mantle lithologies. For simplicity and broad applicability, we only consider a chemically homogeneous mantle source. Details of the phase diagram, governing equations, initialization procedure, and finite volume discretiza-

tion are previously published. Numerical solutions to the discrete system are obtained using the Portable, Extensible Toolkit for Scientific Computation (PETSc, refs. (22, 23)).

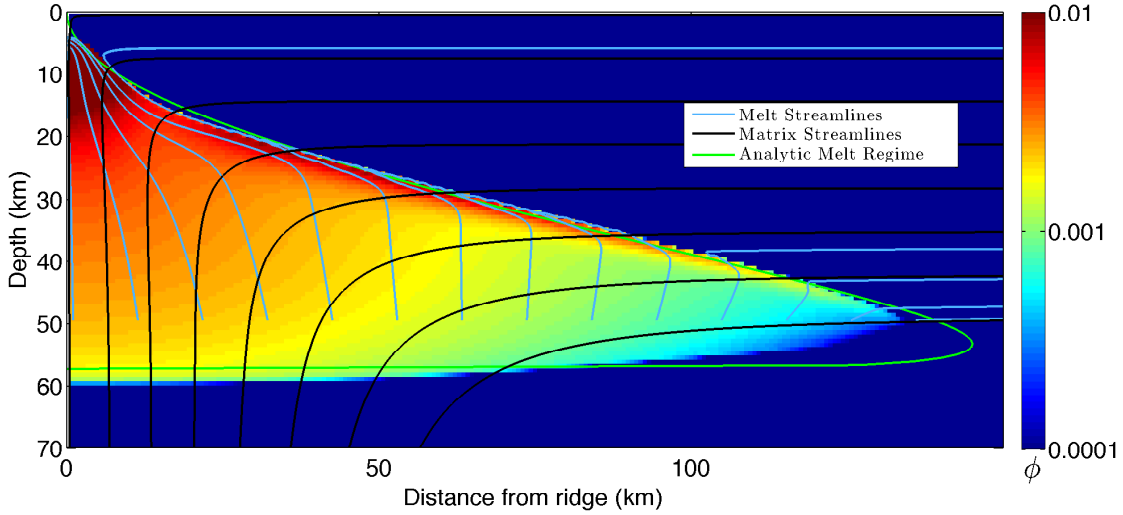


Figure S1: Numerical output for a simulation with a half-spreading rate of 4 cm/yr and permeability factor $K_0 = 10^{-12}$ m². Streamlines for the magma flow (light blue) and mantle matrix (black) are plotted overtop of the porosity (color map). The green line is the analytically determined boundary of the melt regime $x_l(z)$, given by equation (11).

Figure S1 shows the porosity and streamlines (of both solid mantle matrix and magma) from the numerical model of a ridge with a half spreading rate of 4 cm/y. A partially molten region exists at intermediate depths between the high-pressure mantle at depth and the low temperature lithosphere at the surface. Mantle material follows a corner-flow trajectory while most melt is focused towards the ridge. A small portion of melt, produced far from the ridge axis, freezes into the base of the lithosphere and is transported away laterally.

B The reduced model

Analysis of numerical simulations demonstrates that the pressure fluctuations associated with sea level produce only small perturbations to the background, steady-state pattern of melting and melt transport. An approximation of this background regime, which is associated with a constant sea level, thus forms the basis for a reduced complexity model. Sea-level variations are then used in a calculation of melting-rate perturbations; finally, as a leading-order approximation, melting-rate perturbations are transported to the ridge axis according to rates and pathways derived from the unmodified background regime. This approach is adapted from linearized stability analysis (24), but unlike that approach, the reduced models for the background state and perturbations are not obtained by formally solving a linearized system of partial differential equations.

The background state is constructed by combining aspects of the corner-flow solution (25), the half-space cooling model for the lithosphere (26), and a two-component melting model (27). A one-dimensional model (28) of a column of mantle rock is used to determine the rates of melting and melt segregation on the basis of thermodynamic and kinematic parameters of the ridge and mantle system. These solutions, along with a new solution that defines the melting region, are used to solve for the steady state production of melt by upwelling mantle flow. Finally, an approximate expression for the melt travel time to the ridge axis, calculated from the column model, is used to estimate sea-level induced variations in melt production and crustal thickness.

B.1 Melting and melt segregation in the background state

We first describe our approach to predicting the porosity and melt segregation velocity that define the background state. Porosity and melt segregation develop in response to the large scale upwelling and melting beneath ridges. We make several simplifications

and use the one-dimensional column model of Hewitt (15). This model assumes that both melt and solid flow only vertically, and that the two phases are in local thermodynamic equilibrium. Melting rates are determined using conservation principles in the context of a two-component chemical system. For idealized, linear solidus and liquidus relations, approximations of the melting rate, porosity, and fluid velocity may be obtained analytically. For a mantle solidus given by

$$T_S(z) = T_{S_0} - \gamma\rho_mgz + \lambda X_m, \quad (2)$$

the maximum depth of melting z_m is

$$z_m = \frac{T_{S_0} + \lambda X_m - T_m}{\gamma\rho_mg - \alpha g T_m / c} \quad (3)$$

where T_{S_0} is the reference solidus temperature at the surface, γ is the Clausius-Clapeyron slope, λ is the temperature variation associated with changes in composition, X_m and T_m are the composition and potential temperature of the deep mantle respectively, ρ_m is the mantle density, g is the gravitational acceleration, and c is the specific heat. z is a coordinate aligned with gravity that is positive upwards, such that $z = 0$ defines the surface of the solid Earth and $z_m < 0$. The degree of melting, as a function of depth, is

$$F(z) = \frac{\gamma\rho_mgc - \alpha g T_m}{L + c\lambda\Delta X} (z - z_m), \quad (4)$$

where L is the latent heat of melting and ΔX is the compositional difference between the solid and liquid phases. The adiabatic melt productivity of the mantle, in units of kg/m^3 per meter of upwelling (i.e. kg/m^4), can be calculated using equation (4) and is

$$\Pi = \rho_m \frac{dF}{dz} = \rho_m \frac{\gamma\rho_mgc - \alpha g T_m}{L + c\lambda\Delta X}. \quad (5)$$

Using this relation, the degree of melting can be expressed more compactly as $F(z) = \Pi(z - z_m)/\rho_m$. Assuming that compaction stresses may be neglected throughout the

column, the magmatic upwelling rate w_f is given by (15)

$$w_f \approx \left(\frac{K_0 \Delta \rho g}{\phi_0^n \eta_f} \right)^{\frac{1}{n}} \left(\frac{\Pi W_m}{\rho_m} \right)^{1 - \frac{1}{n}} (z - z_m)^{1 - \frac{1}{n}}, \quad (6)$$

where W_m is the upwelling rate of the background mantle, K_0 , ϕ_0 , and n are parameters in the permeability relation

$$K = K_0 \left(\frac{\phi}{\phi_0} \right)^n, \quad (7)$$

ϕ is the porosity, $\Delta \rho$ is the difference in density between the solid and liquid phases, and η_f is the magma viscosity.

B.2 Delineating the region of partial melting

Melting and melt segregation beneath the ridge occur only in the region where temperatures exceed the local solidus temperature. We already know that the base of this region is z_m but in equation (1), we require an expression for the width of the region x_l at any depth. We now develop this expression.

The potential temperature of the mantle $\tilde{T}(x, z)$ in the vicinity of the ridge can be modelled using the half-space cooling solution (26) as

$$\tilde{T}(x, z) = T_m + (T_{\text{sfc}} - T_m) \operatorname{erfc} \left(\frac{|z|}{2} \sqrt{\frac{U_0}{\kappa x}} \right), \quad (8)$$

where κ is the thermal diffusivity, U_0 is the half-spreading rate of the lithosphere at the ridge, T_{sfc} is the surface temperature, and T_m is the mantle potential temperature. The real temperature of the mantle $T(x, z)$ is calculated by adding to eqn. (8) the (linearized) adiabatic temperature gradient $\alpha g T_m z / c$. Furthermore, in regions where melting has occurred, the temperature is reduced by a factor of FL/c , where F is the degree of melt given above in equation (4). With these modifications, the half-space cooling solution

becomes

$$T(x, z) = T_m + (T_{\text{sfc}} - T_m) \operatorname{erfc} \left(\frac{|z|}{2} \sqrt{\frac{U_0}{\kappa x}} \right) - \frac{\alpha g T_m}{c} z - \frac{\Pi L}{\rho c} (z - z_m). \quad (9)$$

Using a mantle solidus temperature (15)

$$T_S(z) = T_{S_0} - \gamma \rho g z + \lambda \chi_m, \quad (10)$$

we can solve for the curve defining the boundary of the melt region $x = x_l(z)$ by setting $T(x_l, z)$ from equation (9) equal to $T_S(z)$. This gives

$$x_l(z) = \frac{U_0 z^2}{4\kappa} \left(\operatorname{erfc}^{-1} \left[\frac{\gamma \rho g - \alpha g T_m / c - \Pi L / \rho c}{T_m - T_{\text{sfc}}} (z - z_m) \right] \right)^{-2}. \quad (11)$$

This can be written compactly as

$$x_l(z) = \frac{U_0}{4\kappa} R(z), \quad (12)$$

where $R(z)$ is a function that depends on the thermodynamic parameters of the mantle but is independent of spreading rate and permeability:

$$R(z) = \left(\frac{z}{\operatorname{erfc}^{-1} \left[\frac{\gamma \rho g - \alpha g T_m / c - \Pi L / \rho c}{T_m - T_{\text{sfc}}} (z - z_m) \right]} \right)^2. \quad (13)$$

Equation (12) demonstrates that the cross-sectional area of the melt region scales linearly with the half-spreading rate.

B.3 The melt transport time

We expect sea-level induced variations in melting rate to be small compared to melting rates associated with upwelling mantle. We therefore assume that the rate of melt segregation, calculated using the column model for the background decompression melting, will remain unchanged. This rate can then be used to calculate the transport time for

perturbations in melt production due to changing sea level. The one-dimensional melt transport rate for a parcel of fluid is $w_f = dz/dt$. Rearranging, integrating, and using equation (6) for the melt speed gives

$$\begin{aligned}
\tau(z) &= \int_z^0 \frac{dz}{w_f(z)}, \\
&= \int_z^0 \left(\frac{\eta_f \phi_0^n}{K_0 \Delta \rho g} \right)^{\frac{1}{n}} \left(\frac{\Pi W_m}{\rho} \right)^{\frac{1}{n}-1} (z - z_m)^{\frac{1}{n}-1} dz, \\
&= n \left(\frac{\eta_f \phi_0^n}{K_0 \Delta \rho g} \right)^{\frac{1}{n}} \left(\frac{\Pi W_m}{\rho} \right)^{\frac{1}{n}-1} \left[(-z_m)^{\frac{1}{n}} - (z - z_m)^{\frac{1}{n}} \right], \\
&= \tau_m \left[1 - \left(1 - \frac{z}{z_m} \right)^{\frac{1}{n}} \right].
\end{aligned} \tag{14}$$

$\tau(z)$ is the time taken for a parcel of material that melts at a depth z to reach the surface. τ_m is the time taken for melt at the base of the melting column ($z = z_m$) to reach the surface and is given by

$$\tau_m = n \left(\frac{\eta_f \phi_0^n}{K_0 \Delta \rho g} \right)^{\frac{1}{n}} \left(\frac{\Pi W_m}{\rho} \right)^{\frac{1}{n}-1} (-z_m)^{\frac{1}{n}}. \tag{15}$$

For simplicity we will assume that the melt travel time is independent of lateral position x and that the solution for a one-dimensional column can be applied independently of lateral position. This assumption simplifies the calculation considerably. More sophisticated transport models are possible, but at the cost of reliance on numerical methods. However, since we already have a full numerical solution to the governing equations, we have sought a reduced model that is computed analytically, captures only the leading-order physics, and is hence easily interpretable.

This simplification excludes two main factors in the melt transport process. It gives no consideration for the lateral flow of melt that would be necessary to focus off-axis melting towards the ridge. (29) demonstrated that a high-porosity boundary layer forms at the base of the lithosphere, creating a channel that rapidly transports melt laterally towards

the ridge axis. Melt is therefore expected to flow sub-vertically beneath the high-porosity boundary layer; the column model represents a reasonable approximation for this flow.

An additional, useful relationship is the depth as a function of delay time. This is given by inverting equation (14) for z and defining $\zeta(\tau)$ as

$$\zeta(\tau) = z_m \left[1 - \left(1 - \frac{\tau}{\tau_m} \right)^n \right]. \quad (16)$$

B.4 Crustal thickness variations due to sea-level change

We now develop a calculation of the effect of changes in sea-level on crustal thickness. Let $S(t)$ represent the sea-level height at time t with respect to some fixed, reference sea level. Pressure variations associated with sea-level changes will, to leading order, be felt equally everywhere beneath the ridge and are assumed to be independent of spatial position in the mantle. The perturbation to the melting rate from sea level change is

$$\Gamma_{SL} = \frac{\rho_w}{\rho_m} \Pi \dot{S}. \quad (17)$$

where $\dot{S} = dS/dt$. Sea-level induced perturbations in melting rate will be transported to the ridge by the background magma flow. A perturbation at time t and position (x, z) will arrive at the ridge and be recorded in the crustal thickness at a time $t + \tau(x, z)$, where $\tau(x, z)$ is the time taken for the melt to travel to the surface. The total melt delivery to the ridge from sea-level induced melting M_{SL} in units of kg/year per meter along the ridge is

$$M_{SL}(t) = \int_{z_m}^0 \int_0^{x_l(z)} \frac{\rho_w}{\rho_m} \Pi \dot{S}(t - \tau(x, z)) \, dx \, dz, \quad (18)$$

where $x_l(z)$ is the distance between the ridge axis and the edge of the melting regime. By assuming that the travel time depends only on the depth z (see sec. B.3, above), we can carry out the inner integral to arrive at the approximate and simpler expression

$$M_{SL}(t) \approx \frac{\rho_w}{\rho_m} \Pi \int_{z_m}^0 x_l(z) \dot{S}(t - \tau(z)) \, dz. \quad (19)$$

To compute the crustal thickness variation associated with this mass delivery rate we divide M_{SL} by the crustal density and the ridge half-spreading rate to give

$$C_{SL}(t) = \frac{\Pi}{U_0} \frac{\rho_w}{\rho_m \rho_c} \int_{z_m}^0 x_l(z) \dot{S}(t - \tau(z)) dz. \quad (20)$$

Equation (20) requires the geometry of the melting region $x_l(z)$ from equation (12) and the travel time for melt produced at depth to rise to the surface $\tau(z)$ from equation (14). The inverse dependence of C_{SL} on U_0 cancels with the linear dependence of x_l on U_0 ; however, admittance in Fig. 2c still depends on spreading rate because of the spreading-rate control on melt travel-time τ (eqns. (14) and (15)).

B.5 A Green's function for crustal thickness perturbations

The crustal thickness response to an instantaneous step-change in sea level is quantified by a Green's function; convolution of this function with an arbitrary sea-level history \dot{S} provides a convenient way to compute the predicted variation in crustal thickness. To calculate the Green's function for the crustal thickness we calculate the response of the system to an instantaneous, unit change in sea level at time $t = 0$. The sea level as a function of time is then $S = S_0 + H(t)$, where $H(t)$ is the Heaviside function (equal to zero for $t < 0$ and one for $t \geq 0$). The rate of change of sea-level is then simply given by the Dirac delta-function,

$$\dot{S} = \delta(t). \quad (21)$$

From equation (20) the crustal thickness is given by

$$C_\delta(t) = \frac{\Pi}{U_0} \frac{\rho_w}{\rho_m \rho_c} \int_{z_m}^0 x_l(z) \dot{S}(t - \tau(z)) dz. \quad (22)$$

Substituting in equations (12) and (21) for $x_l(z)$ and \dot{S} and simplifying gives

$$C_\delta(t) = \frac{\Pi}{4\kappa} \frac{\rho_w}{\rho_m \rho_c} \int_{z_m}^0 R(z) \delta(t - \tau(z)) dz. \quad (23)$$

The integration variable can be switched from depth to time using $dz = \zeta' d\tau$, where $\zeta' = d\zeta/d\tau$ can be calculated from equation (16), giving

$$C_\delta(t) = \frac{\Pi}{4\kappa} \frac{\rho_w}{\rho_m \rho_c} \int_{\tau_m}^0 R(\zeta(\tau)) \delta(t - \tau) \zeta'(\tau) d\tau. \quad (24)$$

Due to the presence of the delta function, the integration can be carried out to give

$$C_\delta(t) = \begin{cases} -\frac{\Pi}{4\kappa} \frac{\rho_w}{\rho_m \rho_c} R(\zeta(t)) \zeta'(t) & \text{for } 0 \leq t \leq \tau_m, \\ 0 & \text{for } t < 0 \text{ and } t > \tau_m. \end{cases} \quad (25)$$

We have assumed that the melting-rate perturbations caused by SL-variation do not alter the background state and hence the crustal response to an arbitrary sea-level history can be obtained by decomposing that history into a series of scaled Dirac delta functions and superposing the response to those impulses. Equation (25) gives the response to an individual impulse, and therefore the solution at time t for an arbitrary sea-level forcing function is

$$C_{SL}(t) = \int_{-\infty}^t C_\delta(t - \tilde{t}) \dot{S}(\tilde{t}) d\tilde{t}. \quad (26)$$

In practice, the limits of integration can be reduced to $[t - \tau_m, t]$ because C_δ is non-zero only in that interval. Equation (26) sums all contributions to the crustal thickness from sea-level change from $t = -\tau_m$ to time t . Then by examination, we find that the Green's function is

$$\mathcal{G}(t, \tilde{t}) = C_\delta(t - \tilde{t}) = -\frac{\Pi}{4\kappa} \frac{\rho_w}{\rho_m \rho_c} R(\zeta(t - \tilde{t})) \zeta'(t - \tilde{t}), \quad (27)$$

where $\zeta(t)$ is given by eqn. (16), $R(\zeta)$ is given by eqn. (13), and $\zeta'(t)$ is obtained by taking the derivative of ζ with respect to τ . The crustal thickness for an arbitrary sea-level forcing is then given by the convolution

$$C_{SL}(t) = \int_{t-\tau_m}^t \mathcal{G}(t, \tilde{t}) \dot{S}(\tilde{t}) d\tilde{t}. \quad (28)$$

B.6 Comparison with the full model

Admittance curves computed with the full, numerical model and with the reduced model are shown in Figures 2(a) and (b), respectively. A key characteristic of these curves is the forcing period at which they reach peak admittance. Figure S2 shows the period at peak admittance for the full and the reduced models. The good agreement indicates that the reduced model captures the physics that controls the magmatic response to sea-level variation.

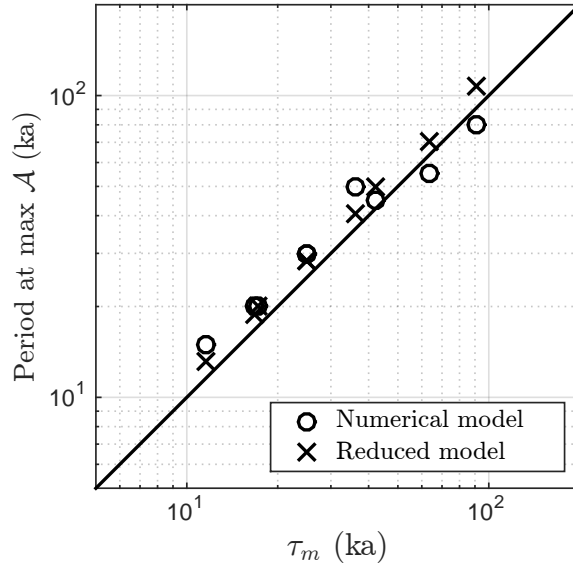


Figure S2: Comparison of the full and reduced model in terms of the sea-level period that gives the maximum admittance \mathcal{A} . The x -axis is the melt transport time computed using the reduced model.

C Bathymetric data acquisition and processing

The icebreaker Araon of the Korean Polar Research Institute is equipped with an EM 122 multi-beam echosounder from Kongsberg for measuring bathymetry. The device uses up to 288 simultaneous beams per swath and operates at about 12 kHz. Data is processed

using the HIPS & SIPS software (version 7.0) of the CARIS company.

D Time-series analysis of bathymetry profiles

We first seek to identify a sequence of bathymetry from the Australian-Antarctic ridge that is broadly representative of the abyssal hill structure at the ridge. Lines traversing the ridge are defined by an Euler pole from the MORVEL plate spreading solution (17) at approximately 1 km intervals. Bathymetry observations are spaced at approximately 50 m in this region and values along the lines are obtained by interpolation using a Delaunay triangulation. Higher resolution sampling of lines has no appreciable influence on the spectral results reported below.

Distance along lines is converted into time in the past by dividing by spreading rate, where the half spreading rate is about 3.3 cm/yr and account is taken of variations associated with distance from the Euler pole. In order to align bathymetry lines, cross-covariance is computed between each successive pair, and the more eastward line is shifted into a position that maximizes covariance. For purposes of aligning the structure of interest, it is useful to filter each line for variations at frequencies outside of those between $1/150 \text{ ky}^{-1}$ and $1/10 \text{ ky}^{-1}$. A zero-phase backward-forward method is used for filtering with a seven-point Butterworth filter. Cross-correlations between successive pairs of filtered and aligned bathymetry lines show a region between 152.9°E and 153.1°E comprising 7 lines whose correlations are all above 0.7. Only two other instances amongst 20 have comparable correlations, suggesting that this region is especially pristine. The aligned but unfiltered versions of these 7 lines are averaged together to form a single time series.

To estimate the center-point of the ridge in the average line, an initial guess of the highest point is selected. For purposes of display, we plot bathymetry from south of

the ridge on the left and northern bathymetry to the right. According to our model, bathymetry variations resulting from changes in sea level should be symmetric across the ridge, and we search within ± 50 ky of the selected high point for a center about which the cross-correlation of the segments north and south of the ridge are maximised. The bathymetry line is again filtered outside of frequencies between $1/150 \text{ ky}^{-1}$ and $1/10 \text{ ky}^{-1}$ in order to focus on frequencies where sea level variability is most energetic. Adding 22 ky to the age of the bathymetry line maximizes cross-correlation across the ridge, giving a value of 0.50, and has the effect of shifting the estimated ridge center southward.

The spectrum of ridge bathymetry is estimated using the multitaper method with seven tapers (18). We focus on the segment south of the ridge because it extends 1310 ky, as opposed to 629 ky north of the ridge, and because the longer duration permits for greater frequency resolution. Spectral energy density strongly increases toward lower frequencies, as follows from the effects of thermal subsidence, the presence of an axial rise, and likely as a consequence of faulting. In order to better identify spectral peaks amidst this red background continuum, time series are pre-whitened prior to spectral analysis by taking the time difference. Pre-whitening gives nearly equivalent results to multiplying unwhitened spectral estimates by frequency squared but has the benefit of making each tapered spectral estimate more independent. It follows that pre-whitening increases the estimated equivalent degrees of freedom from an average of 12.07 to 13.99 at frequencies between $1/150$ and $1/10 \text{ ky}^{-1}$, where the upper bound is 14, or twice the number of tapered spectral estimates.

To assess statistical significance we adopt a null hypothesis of a smoothly varying background spectral energy density that randomly varies according to a chi-squared distribution having the estimated nearly 14 degrees of freedom. The approximate 95th percentile of this null is indicated by the black bar at the upper right of Fig. 3c. Statisti-

cally significant spectral peaks are indicated at frequencies where the estimated spectral energy density rises above the mean background continuum (represented by the dot) by a distance greater than that to the 95th percentile of the null (top of the bar). The lower extension of the bar indicates the distance between the mean and 5th percentile. Note that the use of logarithmic scaling in the ordinate permits for applying this confidence interval with a constant vertical distance because the mean and variance of the chi-square distribution has a constant linear relationship. Spectral peaks at frequencies near the main Pleistocene ice age cycle ($1/100 \text{ ky}^{-1}$), obliquity ($1/41 \text{ ky}^{-1}$), and precession ($1/23 \text{ ky}^{-1}$) are each indicated as being statistically significant, mirroring the spectral peaks predicted by our model in response to sea level variations.

Bathymetry at another section of the Australian-Antarctic ridge 400 km southeast is analysed using the same approach, where 20 lines between 158.7°E and 159.2°E are identified as being especially consistent (see supplementary Fig. S2).

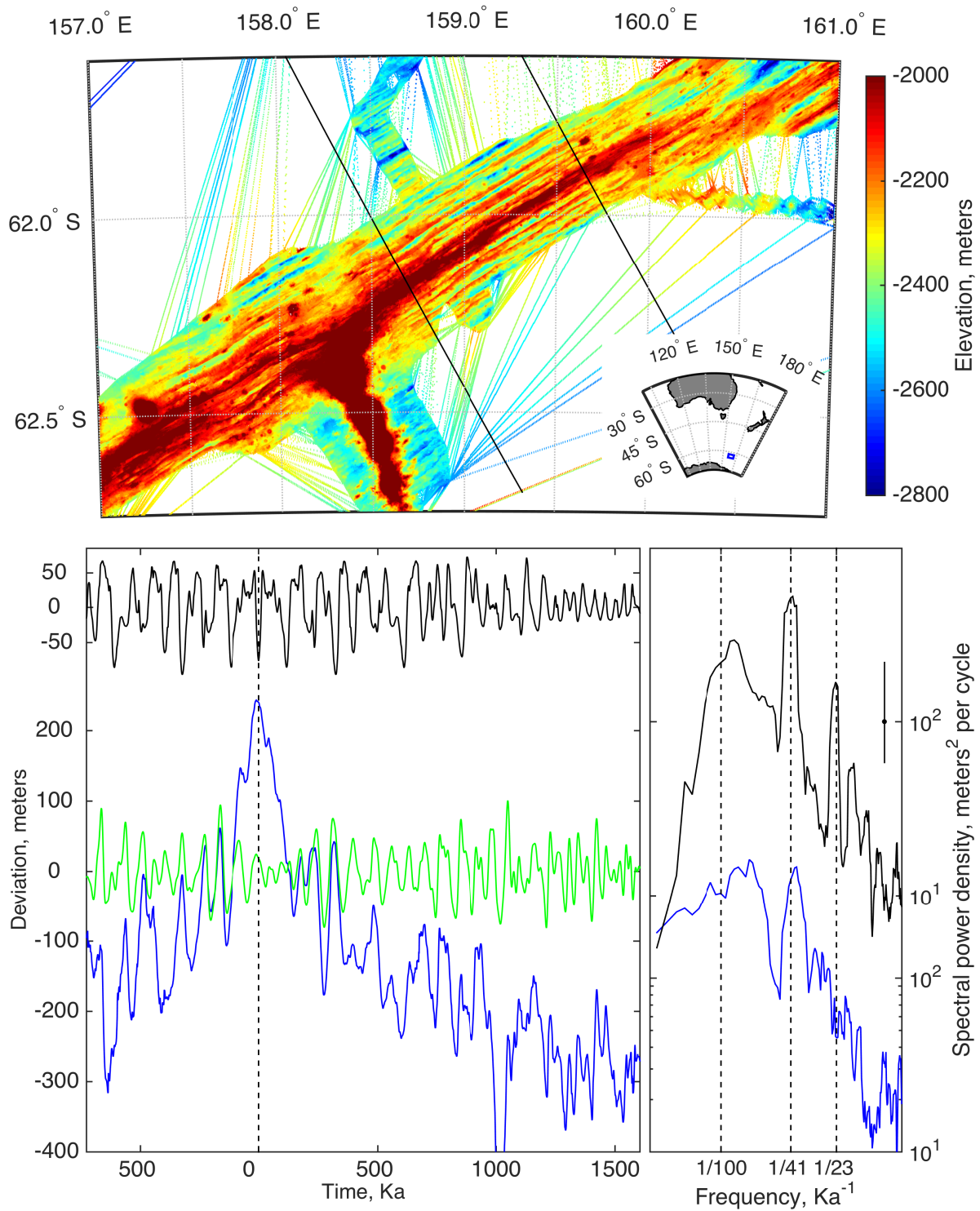


Figure S3: Similar to Fig. 3 but for a section of the Australian-Antarctic Ridge 400 km to the southeast. A region of consistent bathymetry is indicated between the black lines (top) and shown in profile after converting off-axis distance to an estimate of time (bottom left, blue) and after filtering (green). Simulated bathymetry is the same as that shown in Fig. 3 ($U_0 = 3.3$ cm/yr and $K_0 = 10^{-13}$ m²). Spectral estimates (bottom right) are shown for the full bathymetry (blue) and model results (black, offset upward by an order of magnitude).

Parameter	Value	Parameter description
ρ	3000 kg/m ³	Reference density
ρ_w	1000 kg/m ³	Density of water
$\Delta\rho$	500 kg/m ³	Mantle–magma density difference
g	10 m/s ²	Gravitational acceleration
K_0	10 ⁻¹³ m ²	Reference permeability
ϕ_0	0.01	Reference porosity
K	$K_0(\phi/\phi_0)^n$ m ²	Permeability at porosity ϕ
η_l	1 Pa·s	Fluid/melt viscosity
L	4 × 10 ⁵ J/kg	Latent heat
c	1200 J/kg·K	Specific heat
κ	10 ⁻⁶ m ² /s	Thermal diffusivity
α	3 × 10 ⁻⁵ 1/K	Thermal expansion
γ	60 × 10 ⁻⁹ K/Pa	Clapeyron slope
λ	400 K	Solidus change due to composition
χ_m	0.85	Mantle composition
$\Delta\chi$	0.1	Solid-liquid composition difference
T_m	1648 K	Potential temperature of upwelling mantle
T_{s_0}	1565 – $\lambda\chi_m$ K	Reference solidus temperature
W_m	various cm/y	Upwelling mantle velocity
n	3	Exponent in porosity relation
ΔS	–100 m	Sea level change amplitude

Table 1: Parameter values for calculations.

References and Notes

1. H. Menard, J. Mammerickz, Abyssal hills, magnetic anomalies and the east pacific rise. *Earth Planet. Sci. Lett.* **2**, 465–472 (1967). [doi:10.1016/0012-821X\(67\)90191-4](https://doi.org/10.1016/0012-821X(67)90191-4)
2. D. Scheirer, K. C. Macdonald, D. W. Forsyth, S. P. Miller, D. J. Wright, M.-H. Cormier, C. M. Weiland, A map series of the Southern East Pacific Rise and its flanks, 15° S to 19° S. *Mar. Geophys. Res.* **18**, 1–12 (1996). [doi:10.1007/BF00286201](https://doi.org/10.1007/BF00286201)
3. K. Macdonald, P. Fox, R. Alexander, R. Pockalny, P. Gente, Volcanic growth faults and the origin of Pacific abyssal hills. *Nature* **380**, 125–129 (1996). [doi:10.1038/380125a0](https://doi.org/10.1038/380125a0)
4. J. Goff, Y. Ma, A. Shah, J. Cochran, J. Sempere, Stochastic analysis of seafloor morphology on the flank of the Southeast Indian Ridge: The influence of ridge morphology on the formation of abyssal hills. *J. Geophys. Res.* **102** (B7), 15521 (1997). [doi:10.1029/97JB00781](https://doi.org/10.1029/97JB00781)
5. E. Kappel, W. Ryan, Volcanic Episodicity and a Non-Steady State Rift Valley Along Northeast Pacific Spreading Centers: Evidence From Sea MARC I. *J. Geophys. Res.* **91** (B14), 13925 (1986). [doi:10.1029/JB091iB14p13925](https://doi.org/10.1029/JB091iB14p13925)
6. P. Huybers, C. Langmuir, Feedback between deglaciation, volcanism, and atmospheric CO₂. *Earth Planet. Sci. Lett.* **286**, 479–491 (2009). [doi:10.1016/j.epsl.2009.07.014](https://doi.org/10.1016/j.epsl.2009.07.014)
7. D. C. Lund, P. D. Asimow, Does sea level influence mid-ocean ridge magmatism on Milankovitch timescales? *Geochem. Geophys. Geosyst.* **12**, 12009 (2011). [doi:10.1029/2011GC003693](https://doi.org/10.1029/2011GC003693)
8. D. McKenzie, The Generation and Compaction of Partially Molten Rock. *J. Petrol.* **25**, 713–765 (1984). [doi:10.1093/petrology/25.3.713](https://doi.org/10.1093/petrology/25.3.713)
9. R. Katz, *J. Petrol.* **49**, 2099 (2008).
10. R. Katz, *Geochem. Geophys. Geosyst.* **10**, Q0AC07 (2010).
11. R. Katz, S. Weatherley, Consequences of mantle heterogeneity for melt extraction at mid-ocean ridges. *Earth Planet. Sci. Lett.* **335–336**, 226–237 (2012). [doi:10.1016/j.epsl.2012.04.042](https://doi.org/10.1016/j.epsl.2012.04.042)
12. A. Stracke, B. Bourdon, D. McKenzie, Melt extraction in the Earth's mantle: Constraints from U–Th–Pa–Ra studies in oceanic basalts. *Earth Planet. Sci. Lett.* **244**, 97–112 (2006). [doi:10.1016/j.epsl.2006.01.057](https://doi.org/10.1016/j.epsl.2006.01.057)
13. Materials and methods are available as supplementary materials on *Science Online*.
14. M. Siddall, B. Hönisch, C. Waelbroeck, P. Huybers, Changes in deep Pacific temperature during the mid-Pleistocene transition and Quaternary. *Quat. Sci. Rev.* **29**, 170–181 (2010). [doi:10.1016/j.quascirev.2009.05.011](https://doi.org/10.1016/j.quascirev.2009.05.011)
15. I. Hewitt, Modelling melting rates in upwelling mantle. *Earth Planet. Sci. Lett.* **300**, 264–274 (2010). [doi:10.1016/j.epsl.2010.10.010](https://doi.org/10.1016/j.epsl.2010.10.010)
16. J. D. Hays, J. Imbrie, N. J. Shackleton, Variations in the Earth's Orbit: Pacemaker of the Ice Ages. *Science* **194**, 1121–1132 (1976). [Medline doi:10.1126/science.194.4270.1121](https://doi.org/10.1126/science.194.4270.1121)

17. C. DeMets, R. G. Gordon, D. F. Argus, Geologically current plate motions. *Geophys. J. Int.* **181**, 1–80 (2010). [doi:10.1111/j.1365-246X.2009.04491.x](https://doi.org/10.1111/j.1365-246X.2009.04491.x)
18. D. Percival, A. Walden, *Spectral Analysis for Physical Applications: Multitaper and Conventional Univariate Techniques* (Cambridge University Press, 1993).
19. P. Huybers, C. Wunsch, A depth-derived Pleistocene age model: Uncertainty estimates, sedimentation variability, and nonlinear climate change. *Paleoceanography* **19**, PA1028 (2004). [doi:10.1029/2002PA000857](https://doi.org/10.1029/2002PA000857)
20. W. R. Buck, L. L. Lavier, A. N. Poliakov, Modes of faulting at mid-ocean ridges. *Nature* **434**, 719–723 (2005). [Medline doi:10.1038/nature03358](https://doi.org/10.1038/nature03358)
21. J. F. Rudge, D. Bercovici, M. Spiegelman, Disequilibrium melting of a two phase multicomponent mantle. *Geophys. J. Int.* **184**, 699–718 (2011). [doi:10.1111/j.1365-246X.2010.04870.x](https://doi.org/10.1111/j.1365-246X.2010.04870.x)
22. S. Balay *et al.*, www.mcs.anl.gov/petsc (2001).
23. R. Katz, M. Knepley, B. Smith, M. Spiegelman, E. Coon, Numerical simulation of geodynamic processes with the Portable Extensible Toolkit for Scientific Computation. *Phys. Earth Planet. Inter.* **163**, 52–68 (2007). [doi:10.1016/j.pepi.2007.04.016](https://doi.org/10.1016/j.pepi.2007.04.016)
24. M. Tabor, *Chaos and Integrability in Nonlinear Dynamics: An Introduction* (Wiley, 1989).
25. G. Batchelor, *An Introduction to Fluid Mechanics* (Cambridge University Press, 1967).
26. D. Turcotte, G. Schubert, *Geodynamics* (Cambridge University Press, 2002).
27. N. Ribe, The deformation and compaction of partial molten zones. *Geophys. J. R. Astron. Soc.* **83**, 487–501 (1985). [doi:10.1111/j.1365-246X.1985.tb06499.x](https://doi.org/10.1111/j.1365-246X.1985.tb06499.x)
28. I. Hewitt, A. Fowler, Melt channelization in ascending mantle. *J. Geophys. Res.* **114** (B6), B06210 (2009). [doi:10.1029/2008JB006185](https://doi.org/10.1029/2008JB006185)
29. D. Sparks, E. Parmentier, Melt extraction from the mantle beneath spreading centers. *Earth Planet. Sci. Lett.* **105**, 368–377 (1991). [doi:10.1016/0012-821X\(91\)90178-K](https://doi.org/10.1016/0012-821X(91)90178-K)